Atmospheric
Chemistry
and Physics

Research article

In-depth study of the formation processes of single atmospheric particles in the south-eastern margin of the Tibetan Plateau

Li Li[1,3], **Qiyuan Wang**[1,2,3], **Jie Tian**[1], **Huikun Liu**[1], **Yong Zhang**[1], **Steven Sai Hang Ho**[4], **Weikang Ran**[1], **and Junji Cao**[5]

[1]Key Laboratory of Aerosol Chemistry and Physics, State Key Laboratory of Loess and Quaternary Geology, Institute of Earth Environment, Chinese Academy of Sciences, Xi'an 710061, China
[2]CAS Center for Excellence in Quaternary Science and Global Change, Xi'an 710061, China
[3]University of Chinese Academy of Sciences, Beijing 100049, China
[4]Division of Atmospheric Sciences, Desert Research Institute, Reno, NV 89512, United States
[5]Institute of Atmospheric Physics, Chinese Academy of Sciences, Beijing 100029, China

Correspondence: Qiyuan Wang (wangqy@ieecas.cn) and Junji Cao (jjcao@mail.iap.ac.cn)

Abstract. The unique geographical location of the Tibetan Plateau (TP) plays an important role in regulating global climate change, but the impacts of the chemical components and atmospheric processing on the size distribution and mixing state of individual particles are rarely explored in the south-eastern margin of the TP, which is a transport channel for pollutants from Southeast Asia to the TP during the pre-monsoon season. Thus a single-particle aerosol mass spectrometer (SPAMS) was deployed to investigate how the local emissions of chemical composition interact with the transporting particles and assess the mixing state of different particle types and secondary formation in this study. The TP particles were classified into six distinct types, mainly including the largest fraction of the potassium-rich (K-rich) type in the total particles (30.9 %), followed by the biomass burning (BB) type (18.7 %). Most particle types were mainly transported from the sampling site's surroundings and along the Sino-Myanmar border, but the air mass trajectories from north-eastern India and Myanmar show a greater impact on the number fraction of the BB (31.7 %) and dust (18.2 %) types, respectively. Then, the two episodes with high particle concentrations showed that the differences in the meteorological conditions in the same trajectory clusters could cause significant changes in chemical components, especially the dust and aged elemental carbon (aged EC) types, which changed by a total of 93.6 % and 72.0 %, respectively. Ammonium and dust particles distribute at a relatively larger size (~ 600 nm), but the size peak of other types is present at ~ 440 nm. Compared with the abundant sulfate ($^{97}HSO_4^-$), the low nitrate ($^{62}NO_3^-$) internally mixed in TP particles is mainly due to the fact that nitrate is more volatilized during the transport process. The formation mechanism of secondary speciation demonstrates that the formation capacity of atmospheric oxidation is presumably affected by the convective transmission and the regional transport in the TP. However, the relative humidity (RH) could significantly promote the formation of secondary species, especially $^{97}HSO_4^-$ and $^{18}NH_4^+$. This study provides new insights into the particle composition and size, mixing state, and ageing mechanism in high time resolution over the TP region.

1 Introduction

Atmospheric aerosols have complex components and sources and can be coated with inorganic or organic materials during transport and atmospheric processing (Crippa et al., 2013), and then its sizes, chemical compositions, mixing states, and optical properties would change greatly, leading to its influence in the atmosphere being more uncertain (Jacobson, 2002; Zaveri et al., 2010; Matsui, 2016; Budisulistiorini et al., 2017; Ma et al., 2012). Currently, the influences of the complex chemical components on aerosol size and mixing state show large regional differences due to the variations in the pollution sources, atmospheric formation mechanism, and meteorological conditions, which have been widely studied in an urban area at a low altitude (Pratt et al., 2011; Q. Liu et al., 2020; Xu et al., 2017; Wang et al., 2022). However, Q. Liu et al. (2020) have found that the migration or formation of low-volatility components (such as nitrate and organic matter) could effectively be reduced due to evaporation during the upward transportation process, which further alters the chemical compositions and the particle sizes. The transportation of the aerosols to a relatively cleaner environment prevails over the formation of secondary chemicals at a high altitude (D. T. Liu et al., 2020). Therefore, a comprehensive investigation of the detailed characteristics of aerosol formation and mixing states is required to understand their environmental effects at low and high altitudes.

As a typical high-altitude region, the Tibetan Plateau (TP) has the highest and largest mountain area in the world, which is the most sensitive and obvious indicator of climate change on the entire Asian continent (Liu et al., 2017; Chen and Bordoni, 2014; Immerzeel et al., 2010). Numerous studies have shown that the melting and retreat of glaciers in the TP region have been accelerating in recent decades, largely attributed to anthropogenic emissions, such as greenhouse gases and aerosols (Luo et al., 2020; Hua et al., 2019). Atmospheric aerosols can also act as cloud condensation nuclei to impact the local hydrological cycles and monsoon patterns by changing the microphysical properties and life span of clouds (Qian et al., 2011; Gettelman et al., 2013; Kumar et al., 2017). The southern part of the TP is always affected by the transport of more polluted air from South Asia along the mountain valleys, especially during the pre-monsoon (i.e. March–May) with the south-west-prevailing wind (Chan et al., 2017; Zhao et al., 2017; Han et al., 2020). Most studies have focused on the optical characteristics within the TP; however, only little research has been conducted on aerosol components.

Present research on aerosol components over the TP mostly focuses on exploring the influence of light-absorbing carbon aerosols and dust particles on climate change by optical or offline sampling methods (e.g. Q. Y. Wang et al., 2019; Liu et al., 2021). There is a lack of studies on the chemical composition, mixing states, and formation mechanism of aerosols in the south-eastern margin and even the entire TP, especially using high-time-resolution measurements. Although time-integrated sampling with filter collection followed by laboratory analyses has been widely adopted for the chemical characterization of aerosols (C. L. Li et al., 2022; Shen et al., 2015; Zhang et al., 2013), the drawbacks of the traditional approach need to be given attention, including the low time resolution, high detection limit, and time- and labour-intensive procedures. Therefore, more advanced aerosol measurement equipment with high time resolution has been developed; for example the aerosol chemical speciation monitor (ACSM) and aerosol mass spectrometer (AMS) (Ng et al., 2011; Canagaratna et al., 2007) mainly obtained the online data of non-refractory submicron aerosol (including the mass concentration of sulfate, nitrate, ammonium, chloride, and organic matter and the mass spectrum of organic matter). This is beneficial for recognizing the dynamic processes of source emissions of organic matter in the atmosphere (Du et al., 2015; X. Zhang et al., 2019). Meanwhile, aerosol time-of-flight mass spectrometry (ATOFMS) (Dall'Osto et al., 2014) and single-particle aerosol mass spectrometry (SPAMS) (Zhang et al., 2020) are popular for characterizing individual atmospheric particles. These devices can determine the chemical composition and size distribution of the particles in detail and further analyse the dynamic processes of chemical ageing, mixing state, and transport of the particles. (Liang et al., 2022; L. Li et al., 2022a; G. H. Zhang et al., 2019). To the best of our knowledge, the advanced measurement device has not yet been applied for the studies conducted in the TP, leading to a lack of in-depth research on PM$_{2.5}$ pollution in the TP, especially in the south-eastern margin, which hinders our understanding of the distribution characteristics and formation mechanism of aerosol components in high-altitude regions.

The south-eastern margin of the TP is an important transitional zone between the high-altitude TP and the low-altitude Yungui Plateau (Q. Y. Wang et al., 2019; Zhao et al., 2017) and is an ideal place for investigating the impacts of pollutant transport and formation in the high-altitude zone. In this study, continuous field observations of individual particles (SPAMS) were made in the south-eastern margin of the TP during the pre-monsoon period to (i) investigate the changes in chemical characteristics between transport and local fine particles during the pre-monsoon, (ii) determine the size distributions and mixing states of different particle types, and (iii) assess the contributions of photooxidation and aqueous reaction to the formation of the secondary species. These results can expand our understanding of the chemical components, size distribution, mixing state, and ageing pathways of aerosols in the high-altitude areas over the TP and surrounding areas.

2 Methodology

2.1 Sampling site

Intensive 1-month field observations were made on the rooftop (~ 10 m above ground level) of the Lijiang Observatory, Chinese Academy of Sciences (3260 m above sea level; $26°41'24''$ N, $100°10'48''$ E), Gaomeigu County, Yunnan Province, China, during the pre-monsoon period (from 14 April to 13 May 2018). The nearest residential area is the village of Gaomeigu (3–5 km away), with a small population of 113 residents in 27 households. Villagers earn a living by farming (e.g. potato and autumn rape), and biomass is the major domestic fuel (Li et al., 2016). The sampling site is surrounded by rural and mountainous areas and has no obvious industry or traffic emissions. During the total observation period, the average temperature (T) and relative humidity (RH) were $8.4 \pm 3.1\,°C$ and $69 \pm 21\,\%$, respectively. The wind speed (WS) was $2.2 \pm 1.2\,\mathrm{m\,s^{-1}}$, with the prevailing wind in the north and north-east (Fig. S1 in the Supplement).

2.2 Online instrument

A detailed operational principle and the calibrations of the single-particle aerosol mass spectrometer (SPAMS; Hexin Analytical Instrument Co., Ltd., Guangzhou, China) have been described elsewhere (Li et al., 2011). Briefly, individual particles are drawn into the SPAMS through a critical orifice. The particles are focused and accelerated, then aerodynamically sized by two continuous diode Nd:YAG laser beams (532 nm), and subsequently desorbed and ionized by a pulsed laser (266 nm) triggered exactly based on the velocity of the specific particle. The generation of positive and negative molecular fragments is recorded with the corresponding size of individual particles. In summary, a velocity, a detection time, and an ion mass spectrum are recorded for each ionized particle, while there is no mass spectrum for non-ionized particles. The velocity could be converted to d_{va} based on a calibration using polystyrene latex (PSL) spheres (Thermo Scientific Corp., Palo Alto, USA) with predefined sizes. The average ambient pressure is 690 hPa (in a range of 685–694 hPa) during the measurements and calibration. A hollow silicone dryer was installed in front of the inlet. This reduces the uncertainty in particle collection efficiency due to the changes in humidity in sampled airs. Particles measured by the SPAMS mostly have a vacuum aerodynamic diameter (d_{va}) of 0.2–2.0 µm. This SPAMS-specific size distribution is semi-quantitatively evaluated by the relative concentration and contribution of each particle type, mainly due to its large dependence on the particle detection efficiency (Allen et al., 2000; Yang et al., 2017). The characteristics of the SPAMS-specific size distribution are statistical results, while the comparison of the relative distribution and number fraction of different particle types in each size bin is significant.

Meteorological parameters, including the temperature ($°C$), RH ($\%$), WS ($\mathrm{m\,s^{-1}}$), and wind direction (WD), were continuously measured using an automatic weather station (Model MAWS201, Vaisala HydroMet, Helsinki, Finland) at a 5 min resolution, and the planetary boundary layer (PBL) was acquired from the website https://doi.org/10.5065/D6M043C6 (National Centers for Environmental Prediction et al., 2000) at a 1 h resolution. Gaseous concentrations (ppbv) were obtained using a multiple gas analyser (Thermo Scientific Corp.), including ozone (O_3; Model 49i) and nitrogen oxides (NO_x; Model 42i) at a 5 min resolution. The SPAMS and gas analysers were co-located in the same position, and the weather station was uncovered outside ~ 5 m from the sampling house. Time series of SPAMS particles, gaseous concentrations (NO, NO_x, O_3, and CO), and meteorological parameters (PBL, temperature, RH, WD, and WS) are shown in Fig. S2.

2.3 Individual particle classification

During the observation period, a total of 461 876 ambient particles with a size (d_{va}) of 0.2–2.0 µm were collected, including 55 583 in Episode 1 (E1; from 18 April at 08:00 local time (LT) to 19 April at 08:00 LT) and 62 110 in Episode 2 (E2; from 26 April at 17:00 LT to 28 April at 02:00 LT). The analysed particles are classified into 1557 groups using an adaptive resonance theory neural network (ART-2a) with a vigilance factor of 0.8, a learning rate of 0.05, and 20 iterations (Song and Hopke, 1999). Finally, eight major particle cluster types (i.e. potassium-rich (K-rich), biomass burning (BB), organic carbon (OC), ammonium, aged elemental carbon (aged EC), dust, sodium (Na)–potassium (K)–sulfate (S)–nitrate (N)-containing (NaK-SN), and iron (Fe)–lead (Pb)-containing (metal)) with distinct chemical patterns were manually combined, representing $\sim 99.7\,\%$ of the population of the detected particles. The remaining particles are grouped as "other". The characteristics of the positive and negative mass spectra of each particle type are shown in Fig. S3. A detailed description of classification criteria for individual particles and the characteristic ion fragments for each particle type can be found in Sect. S1. The criteria used for searching some of the secondary species in the SPAMS datasets are summarized in Table S2 in the Supplement.

2.4 Trajectory-related analysis

To determine the influence of regional transport on different particles at the south-eastern margin of the TP, the trajectory cluster analysis was carried out using the 72 h backward air mass trajectories at arrival heights of 500 m above ground level. The trajectories were calculated with the Hybrid Single-Particle Lagrangian Integrated Trajectory model (Draxler and Hess, 1998), and the meteorological data were obtained from the Global Data Assimilation System (GDAS; ftp://arlftp.arlhq.noaa.gov/pub/archives/gdas1,

last access: 6 April 2022). The cluster analysis employs a Euclidean-oriented distance definition to differentiate and cluster the major spatial features of the inputting trajectories. Details of the trajectory-clustering method can be found in Sirois and Bottenheim (1995). To investigate the effects of transport on the chemical characteristics of the individual particles, trajectories with particle number concentrations higher than the 75th percentile are considered to be pollution (Liu et al., 2021).

3 Results and discussion

3.1 Characteristics of particle composition

Table 1 summarizes the number concentrations, relative percentages, and characteristic ions of each particle type. The most dominant particle type in Gaomeigu during the premonsoon is K-rich, accounting for an average of 30.9 % of the total resolved particles, followed by BB (18.7 %), OC (12.8 %), ammonium (11.9 %), aged EC (10.9 %), and dust (10.7 %). Their characteristics of mass spectrum and possible sources are described in Sect. S1 in detail. Similar to the results of some studies in urban areas, the K-rich or carbon-containing types are the dominant particle types (15 %–50 %) (Xu et al., 2018; H. L. Wang et al., 2019; L. Li et al., 2022). Based on a combination of previous studies and the characteristics of the mass spectrum (Fig. S3a) in this study, the K-rich particles are contributed by biomass burning and traffic emissions, as evidenced by these extensive works usually identifying abundant $^{39}K^+$ signals for biomass burning (Pratt et al., 2011; Chen et al., 2017), while the presence of phosphate (m/z $^{79}PO_3^-$) indicates vehicle exhaust (Yang et al., 2017). The results of the correlation between seven variables (Fig. S4) show that the K-rich type is strongly correlated with the ammonium ($r = 0.84$) and aged-EC ($r = 0.90$) types and is well correlated with the OC ($r = 0.70$) and BB ($r = 0.68$) types, further demonstrating that the K-rich particle type is from traffic emissions and biomass burning and is affected by secondary formation during atmospheric ageing in the south-eastern TP. It is worth noting that little research has captured the high proportion of ammonium particles as shown in this study (Shen et al., 2017; Xu et al., 2018), which is ascribed to the conversion of the ammonia (NH_3) precursor emitted from large-scale agricultural activities and mountain forests (Engling et al., 2011; Li et al., 2013). It is necessary to point out that 60 % of ammonium particles contain signals of amine fragment (m/z 58, $C_2H_5NH = CH_2^+$), implying their similar formation pathway (Zhang et al., 2012). Moreover, the amine-containing particles represented 12.5 % of the total ambient particles, which is significantly higher than in some urban areas at low altitudes (around 2 %) (Cahill et al., 2012; Zhang et al., 2015; Li et al., 2017) but is comparable to observed sites with high RH or during fog and cloud events at a high altitude (> 9 %) (Roth et al., 2016; Lin et al., 2019). This suggests that the formation of amines under high-RH

and high-fog conditions might exist in the Gaomeigu area (with an altitude of 3260 m); for example, the high relative fraction of amine-containing particles corresponds to a high RH (Fig. S5), and the existence of amine sources governs the ammonium formation (Bi et al., 2016; Rehbein et al., 2011). The relatively larger fraction of dust particles is related to the short occurrences of dust events in spring (Fig. S6), leading to a wide contribution ranging between 10 % and 70 % in the period of 19:00 LT on 16 April to 10:00 LT on 17 April.

Figure 1 shows the diurnal variations in each particle type. The K-rich, BB, and OC particles decrease after midnight until 06:00 LT, possibly explained by the curtailment of local traffic and biomass burning activities at nighttime even though both the PBL height and WS decrease (Fig. S7). Then, their concentrations rapidly increase in the morning (around 07:00 LT) due to more pollutants from biomass burning and traffic emissions in the upwind region. The increases in PBL height and WS also lead to the transport of air pollutants from the surrounding regions to the sampling site (Liu et al., 2021). At 11:00 LT, the particle concentrations sharply decrease until 16:00–17:00 LT, caused by the pollutant dispersion with continuing increases in the PBL height and WS. Increasing trends are observed after 17:00 LT due to the pollutant accumulation with the reduction in PBL height and WS. In contrast, the ammonium, aged-EC, and dust particles show a unimodal pattern of the daily diurnal variation (Fig. 1d–f). From 00:00 to 06:00 LT, minor fluctuations in particle concentrations of ammonium, aged-EC, and dust particles are observed. After that, their levels continuously elevate until ∼11:00 LT due to the regional transport, traffic emissions, and fugitive dust (refer to Sect. S2). While the PBL height and WS increase continuously, the ammonium, aged-EC, and dust types decline from 12:00 to 17:00 LT. The subsequent increases in these three types after 17:00 LT are attributed to the reduction in PBL height as a result of the accumulation of pollutants in the near-surface atmosphere.

Based on the transport pathways, four air mass clusters are identified to investigate the effect of regional transport on the major particle types (i.e. K-rich, BB, OC, ammonium, aged EC, and dust) (Fig. 2). Clusters 1, 3, and 4 originated from north-eastern Myanmar, accounting for 59.8 %, 33.2 %, and 4.6 % of the total trajectories, respectively. Cluster 1 had an average percentage of 32.7 %, 18.5 %, 12.0 %, 12.5 %, 11.1 %, and 8.9 %, respectively, for the K-rich, BB, OC, ammonium, aged-EC, and dust particles (Table S1). Clusters 3 and 4 have comparable contributions of OC (15.5 % and 12.5 %, respectively) and increased BB (19.3 % and 26.8 %, respectively) as well as decreased K-rich (26.8 % and 25.2 %, respectively), ammonium (10.4 % and 7.7 %, respectively), and aged-EC (7.7 % and 6.3 %, respectively) particles compared to those of Cluster 1, but with a high contribution of dust (16.6 %), which suggests that Clusters 3 and 4 are significantly correlated with dust and biomass burning pollution. However, Cluster 1 is more influenced by compound pollution, mainly including secondary formation, biomass burn-

Table 1. The number concentrations, average percentages, and characteristic ions of nine types of particles during the entire campaign and the average percentages of the six major particle types during two episodes.

Type	Number count	Fraction in total (%)	Episode 1 (%)	Episode 2 (%)	Tracer ions
K-rich	151 040	30.9	29.0	39.3	$^{39}K^+$, $^{26}CN^-$, $^{42}CNO^-$, $^{46}NO_2^-$, $^{62}NO_3^-$, $^{97}HSO_4^-$
BB	91 322	18.7	11.5	14.2	$^{39}K^+$, levoglucosan ($^{45}CHO_2^-$, $^{59}C_2H_3O_2^-$, $^{71}C_3H_3O_2^-$, $^{73}C_3HO_3^-$), $^{26}CN^-$, $^{35,37}Cl^-$, $^{42}CNO^-$, $^{46}NO_2^-$, $^{62}NO_3^-$, $^{97}HSO_4^-$
OC	62 446	12.8	8.1	10.0	$^{27}C_2H_3^+$, $^{37}C_3H^+$, $^{38}C_3H_2^+$, $^{39}K^+/C_3H_3^+$, $^{43}C_2H_3O^+$, $^{51}C_4H_3^+$, $^{26}CN^-$, $^{42}CNO^-$, $^{46}NO_2^-$, $^{62}NO_3^-$, $^{97}HSO_4^-$
Ammonium	58 317	11.9	17.5	13.5	$^{12}C^+$, $^{18}NH_4^+$, $^{39}K^+$, $^{58}C_2H_5NHCH_2^+$, $^{97}HSO_4^-$, $^{195}H(HSO_4)_2^-$
Aged EC	53 337	10.9	10.0	17.2	$C_n^\pm$ ($n = 1$–5), $^{39}K^+$, $^{97}HSO_4^-$
Dust	52 533	10.7	20.3	1.3	$^{40}Ca^+$, $^{56}CaO^+$, $^{16}O^-$, $^{17}OH^-$, $^{76}SiO_3^-$, $^{79}PO_3^-$
NaK-SN	13 726	2.8	NA	NA	$^{23}Na^+$, $^{39}K^+$, $^{62}NO_3^-$, $^{97}HSO_4^-$
Metal	4672	1.0	NA	NA	$^{51}V^+$, $^{56}Fe^+$, $^{64,66,68}Zn^+$, $^{206,207,208}Pb^+$
Others	1580	0.3	NA	NA	No obvious characteristic peaks

NA: not available.
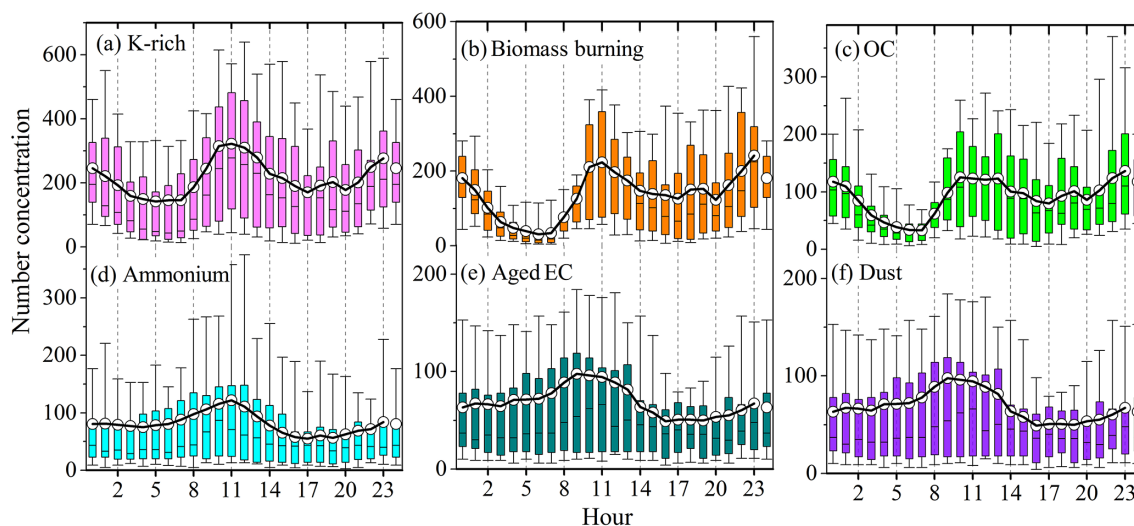
Figure 1. Diurnal box-and-whisker plots of the number concentration of the main particle types (at an hourly resolution): **(a)** potassium (K)-rich, **(b)** biomass burning (BB), **(c)** organic carbon (OC), **(d)** ammonium, **(e)** aged elemental carbon (EC), and **(f)** dust. The lower, middle, and upper lines of the boxes denote the 25th, 50th, and 75th percentiles. The lower and upper whiskers represent the 10th and 90th percentiles, respectively. Average values are shown by white dots.

ing, and traffic emissions. The diurnal variations in the BB and OC fractions are similar and rapidly elevate at 07:00 LT (Fig. S8) due to the increased contribution of biomass burning and traffic emissions from Cluster 1 and ammonium and aged-EC particles (peak at 07:00 LT) caused by the effect of Clusters 1 and 3 together. A stable diurnal variation in the K-rich fraction is mainly due to its large proportion and diverse sources. The similar diurnal trends of Clusters 3 and 4 are both associated with dust contributions, which de-

crease at 04:00 LT and increase at noon. The increased nighttime particles could be attributed to the pollutant accumulation with decreased PBL height. Cluster 2 originates from north-eastern India and passes over Bangladesh. This cluster accounts for only 2.4 % of the total trajectories, of which ∼ 30.8 % and ∼ 35.9 % are mainly associated with the K-rich and BB particles, respectively. Although Clusters 2 and 4 are composed of a small fraction of total trajectories (2.4 % and 4.6 %, respectively), BB and dust particles are identi-

fied as the major pollutants, suggesting significant influences from India and north-eastern Myanmar during the campaign.

A more in-depth investigation of the characteristics of the main particle types in the south-eastern Tibet Plateau was conducted during two episodes when the number concentration of particles was high (E1: from 08:00 LT on 18 April to 08:00 LT on 19 April 2018; E2: 17:00 LT on 26 April to 02:00 LT on 28 April 2018) (Fig. S6). Even though the two episodes are caused by Cluster 1, the chemical components show significant differences (Table 1). During E1, the average fractions of the K-rich, BB, OC, ammonium, aged-EC, and dust particles are 29.0 %, 11.5 %, 8.1 %, 17.5 %, 10.0 %, and 20.3 %, respectively, different from 39.3 %, 14.2 %, 10.0 %, 13.5 %, 17.2 %, and 1.3 %, respectively, during E2. It can be seen that the major changed factor of the dust particles is 93.6 % lower during E2 than E1, and that of the opposite aged-EC particles is 72.0 % higher than E1. Meanwhile, K-rich, BB, and OC particles also increase by 35.5 %, 23.5 %, and 23.4 %, respectively, during E1 compared to E2. For the air mass clusters (Fig. S9), E1 and E2 exhibit minor differences, mostly originating from northern Myanmar and the Sino-Burmese border, but not identical regions. The dust particles that are much lower during E2 than E1 could be explained by higher WS (on average $2.7 \pm 1.0\,\mathrm{m\,s^{-1}}$ versus $0.4 \pm 0.5\,\mathrm{m\,s^{-1}}$) (Fig. S9) and PBL height ($771 \pm 717\,\mathrm{m}$ versus $560 \pm 549\,\mathrm{m}$) (Fig. S10). The dust particles are mainly formed by re-suspension in the local areas. In addition, quickly thrown-up dust belongs to the category of more coarse particles, which are out of the detection range of the SPAMS. However, because the larger dust particles deposited more easily under low-WS and stagnant-air conditions during E1, more suspended dust particles of small size fall within the detection range of the SPAMS. Moreover, the increased PBL height and WS could speed up the transportation of pollutants from multiple sources (e.g. traffic and biomass burning emissions) to the observation site, leading to elevation of the fraction of aged-EC, K-rich, BB, and OC particles during E2. The decreased ammonium fraction during E2 is potentially explained by the reductions in the secondary pollutant formation with declines in RH (from $73.9 \pm 23.9\,\%$ to $53.1 \pm 14.9\,\%$), in comparison to those during E1.

3.2 Characteristics of the SPAMS-specific size distribution and mixing state

The SPAMS-specific size distributions of all particle types are shown in Fig. 3. According to the characteristics of the average mass spectra (refer to Sect. S1 and Fig. S3), the K-rich, BB, OC, and aged-EC particles originated from similar sources of solid-fuel combustion or vehicle emissions. Their SPAMS-specific size is thus distributed within a small scale ($\sim 440\,\mathrm{nm}$) (Fig. S11a). However, the relative percentage of each particle type is distinct, with different size ranges, possibly due to the unique atmospheric processing. For example, as shown in Fig. 3a, the proportions of the K-rich

and BB types increase along with an increase in particle size from 200 to 420 nm, and then they decrease. The OC and aged-EC types are mainly distributed in relatively small sizes, and their proportions gradually decrease when the size ranges become larger. The ammonium and dust types are mainly distributed in large sizes of $\sim 600\,\mathrm{nm}$ (Fig. S11a). The proportion of ammonium particles gradually increases with an increase in particle size and peaks at 740 nm; the relatively large SPAMS-specific size distribution is ascribed to the intense atmospheric ageing during regional transport (refer to Sect. S1). The proportion of dust particles gradually increases with a size > 560 nm and peaks at 1.48 µm. This is consistent with the fact that dust is a coarse particle, generally associated with fugitive dust.

Compared with the SPAMS-specific size distribution of the total particles, the peak values of the six main particle types show minor differences (< 80 nm) during the two different episodes (Fig. 11b, c). However, the percentage of the six particle types is distributed in wider size ranges during E2 than during E1, possibly due to the more intense atmospheric ageing. Similarly, during the two episodes (Fig. 3b, c), the relatively high fractions of the K-rich and BB particles are more affected by the primary emissions when their peak values of the SPAMS-specific size distribution concentrate at < 300 nm, and size distributions > 300 nm are more related to the ageing process (L. Li et al., 2022a; Bi et al., 2011). Relatively greater fluctuation for the large-sized fractions (> 1.1 µm) could be explained by the low particle concentration (a number less than 20). It should be pointed out that further application of this method would require a co-located particle-sizing instrument to scale the size-resolved particle detection efficiency. Both particle composition and size dependence are the predominant impacting factors in the particle detection efficiency of the SPAMS (Wenzel et al., 2003; Yang et al., 2017; Healy et al., 2013).

To investigate the mixing state of the secondary species in the six main particle types, the number fractions of six secondary markers ($^{97}\mathrm{HSO_4^-}$, $^{195}\mathrm{H(HSO_4)_2^-}$, $^{62}\mathrm{NO_3^-}$, $^{18}\mathrm{NH_4^+}$, $^{58}\mathrm{C_2H_5NHCH_2^+}$, and $^{89}\mathrm{HC_2O_4^-}$) are calculated (Fig. 4). The presence of amine ($m/z\ ^{58}\mathrm{C_2H_5NHCH_2^+}$) and sulfuric acid ($m/z\ ^{195}\mathrm{H(HSO_4)_2^-}$) signals is possibly indicative of the water uptake (Chen et al., 2019) and acidic properties of the particles (Rehbein et al., 2011), respectively. The mixing states are obtained by the ratio of the number concentration of the selected ions in each particle type.

The most abundant $^{97}\mathrm{HSO_4^-}$ and $^{18}\mathrm{NH_4^+}$ fractions are seen in ammonium (99 % and 94 %, respectively) and aged-EC (92 % and 31 %, respectively) particles, whereas a very low fraction of $^{62}\mathrm{NO_3^-}$ is found (2 % and 7 %, respectively). These values indicate that ammonium sulfate is the predominant form rather than ammonium nitrate. (Zhang et al., 2013). The high contribution of $^{97}\mathrm{HSO_4^-}$ in EC-containing particles also suggests a significant influence of anthropogenically emitted sulfate precursors (e.g. SO₂) on the ageing of EC-containing particles at high altitudes (Peng
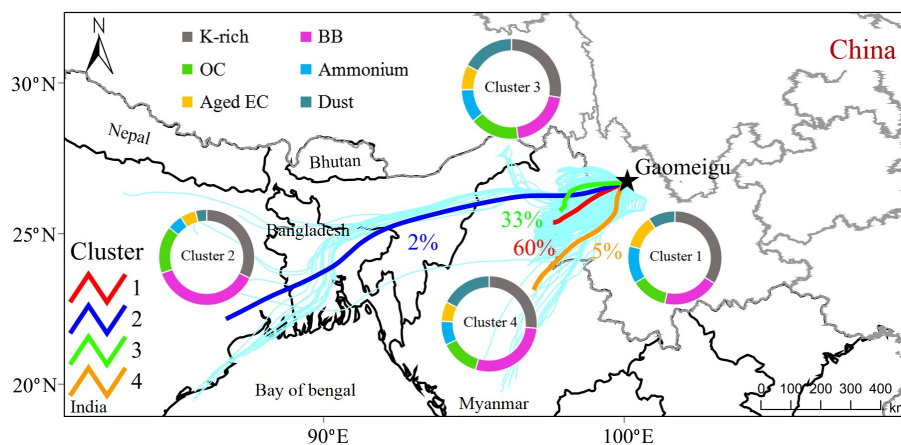
Figure 2. Maps of the mean HYSPLIT back-trajectory clusters (72 h) at a height of 500 m during the whole field observation. The embedded pie chart represents the relative fraction of each particle type in the four clusters.
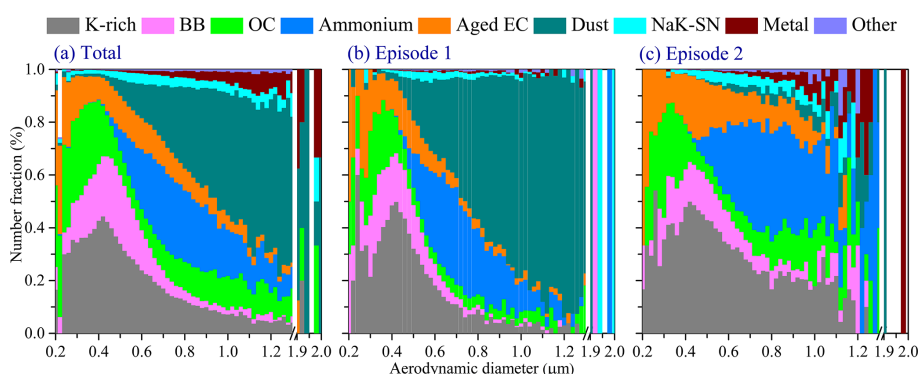
Figure 3. SPAMS-specific size distributions of the relative number fraction (%) of the total particles for nine groups during **(a)** the total sampling campaign and the two episodes **(b)** E1 and **(c)** E2.

et al., 2016; J. K. Zhang et al., 2017). Meanwhile, relatively high number fractions of $^{195}H(HSO_4)_2^-$ and $^{58}C_2H_5NHCH_2^+$ are also observed in ammonium (63 % and 60 %) and aged-EC (4 % and 19 %) particles. These abundant mixtures potentially represent the high hygroscopicity of ammonium and aged-EC particles and their ability to neutralize the acidic particles of ammonium particles (Sorooshian et al., 2007). Then, a moderate fraction of $^{97}HSO_4^-$ and $^{18}NH_4^+$ is seen in the K-rich (65 %, 7 %) and OC (56 %, 4 %) particles. In contrast, a higher $^{62}NO_3^-$ fraction contributes to the K-rich (38 %) and OC (68 %) particles, mainly affected by vehicle emissions and biomass burning (refer to Sect. S1). A relatively low fraction of $^{97}HSO_4^-$ contributes to BB (18 %) and OC (6 %) particles, and the moderate $^{62}NO_3^-$ fraction mixes in BB (45 %) particles but only accounts for 3 % of dust particles. Combined with the results of the minor $^{18}NH_4^+$ fraction (< 1 %) in BB and dust particles, this suggests a relatively low degree of ageing. In addition, oxalate ($^{89}HC_2O_4^-$), a representative component of secondary organic formation, is mainly mixed with BB (13 %) and K-rich (12 %) particles. This is because the substantial precursors of oxalic acid,

including acetate ($^{59}C_2H_3O_2^-$), methylglyoxal ($^{71}C_3H_3O_2^-$), and glyoxylate ($^{73}C_2HO_3^-$), are emitted from biomass burning, and then oxalate heterogeneously forms in BB-related particles (G. H. Zhang et al., 2019; Zauscher et al., 2013). A relatively low fraction (< 5 %) of oxalate-containing particles in OC, ammonium, aged-EC, and dust particles is potentially limited by the contributions of precursor oxalic acid.

Compared to the mixing state of individual particles in urban or suburban areas that are located close to emission sources (Chen et al., 2016; Dall'Osto and Harrison, 2012; J. K. Zhang et al., 2017; L. Li et al., 2022a), the high fractions of sulfate and ammonium in high-altitude areas demonstrate a high degree of ageing of the individual particles, whereas the low fraction of nitrate with high volatility indicates its loss during transportation processing.

The number fractions of six markers in the four trajectories were used to further investigate the impacts of regional transport. As shown in Fig. 5a and c, the dominant mixing ion types in each particle (except for dust) are similar among the four clusters. For Cluster 1, the number fractions of $^{97}HSO_4^-$ and $^{89}HC_2O_4^-$ have larger values in five particle types (ex-
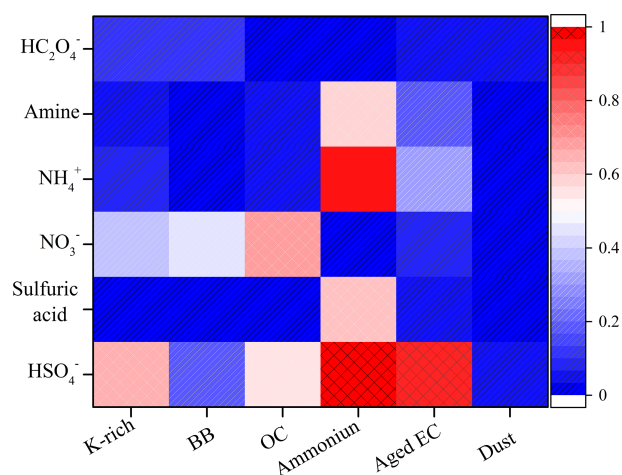
Figure 4. Number fractions of secondary markers associated with the six particle types (K-rich, BB, OC, ammonium, aged EC, dust) during the whole observation. Secondary species include sulfate ($^{97}HSO_4^-$), sulfuric acid ($^{195}H(HSO_4)_2^-$), nitrate ($^{62}NO_3^-$), ammonium ($^{18}NH_4^+$), amine ($^{58}C_2H_5NHCH_2^+$), and oxalate ($^{89}HC_2O_4^-$) ions.

cept for the dust type) than those in other trajectories. Similar to Cluster 1, Clusters 3 and 4 are impacted by regional transport from north-eastern Myanmar, and the fractions of the six markers are also similar in the OC, ammonium, and aged-EC types. However, $^{97}HSO_4^-$ in Clusters 3 and 4 is reduced in the K-rich, BB, and dust types, while $^{62}NO_3^-$ is increased in the K-rich type and decreased in the dust type, compared with Cluster 1. As discussed in Sect. 3.1, these results demonstrate that the ageing degree of Clusters 3 and 4 might be lower than that of Cluster 1. For Cluster 2, the fraction of $^{97}HSO_4^-$ is obviously decreased in the K-rich, BB, and aged-EC types but slightly increased in the dust type (Fig. 5f). However the fraction of $^{62}NO_3^-$ is increased in the K-rich, OC, and dust particles in Clusters 2 compared with Clusters 1, 3, and 4. These variations in Cluster 2 are more likely due to the influences of biomass burning activities from surrounding the sampling site rather than regional transport. Furthermore, Cluster 2 is associated with regional transport from north-eastern India from the afternoon to nighttime (from 15:00 LT on 11 May to 07:00 LT on 12 May), which is favourable to the nitrate formation of N_2O_5 by heterogeneous hydrolysis (Wang et al., 2017; Ding et al., 2021). However, these cases are infrequent, as only 2 % of trajectories are associated with Cluster 2.

During E1, $^{97}HSO_4^-$ fractions greater than 50 % are mixed in the K-rich (81 %), OC (62 %), ammonium (100 %), and aged-EC (98 %) particles (Fig. S12) as well as the low-BB (37 %) and dust (4 %) particles. Unlike with E1, the number fraction of $^{97}HSO_4^-$ in dust increases to 34 % during E2, potentially associated with the enhancement by secondary formation during regional transport. However, the mixing states of $^{195}H(HSO_4)_2^-$, $^{62}NO_3^-$, NH_4^+, and oxalate fractions

are similar between the two episodes. The $^{58}C_2H_5NHCH_2^+$ fractions are significantly higher in E2 than E1 for ammonium (67 % versus 31 %) and aged-EC particles (48 % versus 17 %), due to the relatively higher-hygroscopicity behaviour (i.e. RHs) (Sorooshian et al., 2007).

3.3 Formation process of the high-particle-number-concentration episodes

Photochemical oxidation and aqueous-phase reaction are the key formation pathways of secondary species (Link et al., 2017; Xue et al., 2014; Jiang et al., 2019). The oxidant O_x ($O_3 + NO_2$) concentration and RH usually serve as indicators of the degree of photochemical oxidation (Wood et al., 2010) and aqueous-phase reaction (Ervens et al., 2011), respectively, though the current O_x and RH conditions obtained using the in situ measurement are not indicative of the past conditions experienced by the particle. Thus, the relative number fractions of $^{43}C_2H_3O^+$-, $^{89}HC_2O_4^-$-, $^{62}NO_3^-$-, $^{97}HSO_4^-$-, and $^{18}NH_4^+$-containing particles of the total detected particles were selected to provide a rough estimate of the secondary-formation mechanism under ambient TP conditions (Liang et al., 2022). The correlations of the number fraction of each secondary species with the O_x concentrations (O_x) during daytime (from 06:00 to 20:00 LT) and RH during nighttime (from 20:00 to 06:00 LT the next day) are used to reveal the formation pathways during the two episodes (L. Li et al., 2022).

As illustrated in Fig. 6, for E1, $^{43}C_2H_3O^+$, $^{89}HC_2O_4^-$, $^{97}HSO_4^-$, and $^{18}NH_4^+$ show significant negative linear correlations with O_x ($p < 0.01$), and the correlation strengths range from moderate to strong ($r = -0.51$ to -0.81). However, the $^{62}NO_3^-$ fraction shows an upward trend with an insignificant correlation ($r = 0.33$, $p > 0.05$) with the increase in O_x concentration. For E2, $^{43}C_2H_3O^+$ shows weak correlation with O_x ($r = 0.37$, $p > 0.05$) but strong correlations with $^{89}HC_2O_4^-$, $^{97}HSO_4^-$, and $^{18}NH_4^+$ ($r = 0.81$–0.92, $p < 0.01$). It should be noted that $^{62}NO_3^-$ has a strong negative correlation ($r = -0.85$, $p < 0.01$) with O_x. In general, the opposite linear relationship between secondary aerosol and O_x during E1 and E2 might be influenced by (i) the relatively low secondary formations because of the small number of precursors emitted from anthropogenic activities around the sampling site (Li et al., 2016); (ii) the higher dilution rate of the particles formed in the atmosphere with the more rapid rise in PBL height during E1 than E2 (Fig. S13a); and (iii) the degrees of contribution of regional transport due to the low WS (0.5 ± 0.6 m s^{-1}) during E1 and the high WS (3.1 ± 1.0 m s^{-1}) during E2, respectively (Fig. S9). Therefore, for E1, the increases in the NO_3^- fraction could be influenced by the local nitrate formation, while the declines in other secondary components should be ascribed to the reduced contribution of regional transport. For E2, the decrease in the NO_3^- fraction could be caused by the relatively higher volatilization loss of nitrate than other components
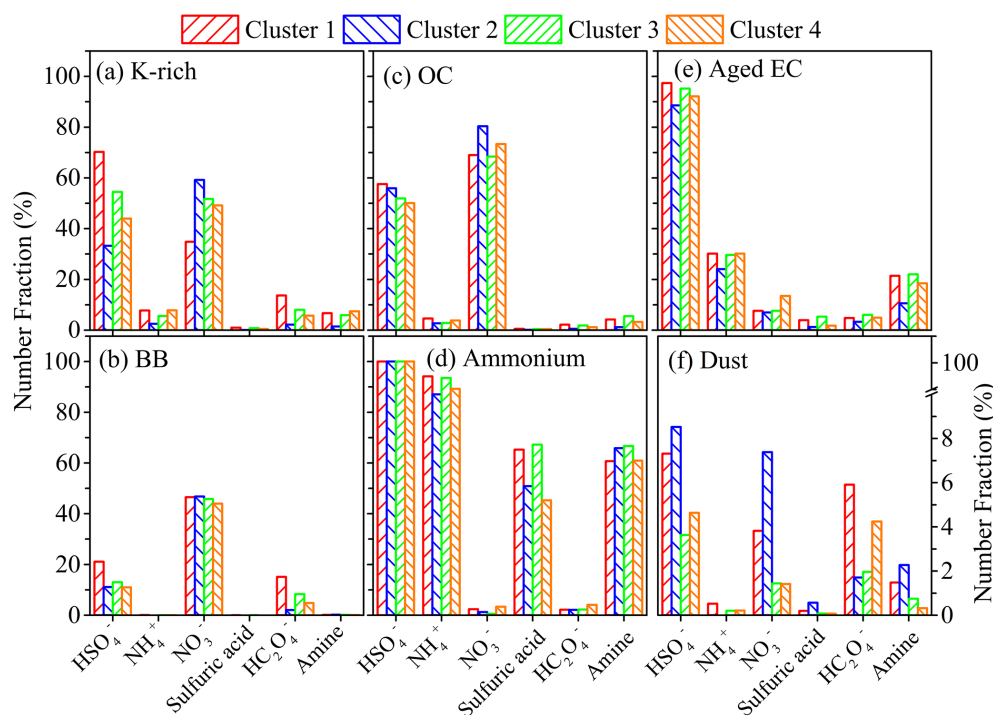
Figure 5. Number fractions of secondary markers associated with the six particle types (i.e. K-rich, BB, OC, ammonium, aged EC, and dust) in four clusters. Secondary species abbreviations as in Fig. 4.

through the regional transport. Additionally, previous work proves that the formations of organic nitrate species (such as $^{27}CHN^+$, $^{30}NO^+$, $^{43}CHO_1N^+$, and CHO_xN^+) through the $NO + RO_2$ pathway dominate 80 % of the total nitrate production in tropical forested regions during summertime (Alexander et al., 2009). Aruffo et al. (2022) also found that low NO_x (i.e. < 6 ppbv), compared to 2.3 ± 0.8 ppbv in this study, could even promote the particle-phase partitioning of the lower volatility of organonitrates. These results suggest that the secondary organic species have different formation capacities through photooxidation reactions, among which the rate of HSO_4^- formation (slope $= 0.017$) is the highest. With increased O_x concentration during E2, the concentration levels of secondary organic species of $C_2H_3O^+$ (18 %–28 %) imperceptibly rise, while the oxalate fraction significantly increases by 7 %–20 %.

Considering that the oxalate is abundantly mixed in K-rich (14 %), BB (15 %), aged-EC (5 %), and dust (6 %) particles in Cluster 1 (Fig. 5) and considering the increased contributions of the K-rich (39.3 %), BB (14.2 %), and aged-EC (17.2 %) types during E2 (Table 1), the apparent formation of oxalate might be due to the enhancement of regional transport. Particularly, this shows that the nearby biomass burning and combustion activities produce more precursor species of oxalate (Sullivan et al., 2007; Kundu et al., 2010; G. Zhang et al., 2017).

Figure 7 illustrates that the number fractions of $^{43}C_2H_3O^+$, $^{89}HC_2O_4^-$, $^{97}HSO_4^-$, and $^{18}NH_4^+$ have moder-

ate to strong positive correlations with RH ($r = 0.70$–0.81, $p < 0.01$ or 0.05) in the nighttime during the two episodes, except $^{43}C_2H_3O^+$ during E2 ($p = 0.48$) and $^{89}HC_2O_4^-$ during E1 ($p = 0.12$). Furthermore, the $^{62}NO_3^-$ fraction has no obvious changes, with insignificant correlation with RH during E1 ($p = 0.43$), and presents a moderate negative correlation with RH ($r = 0.69$, $p < 0.01$) during E2. As shown in Fig. 7e, the highest aqueous formation rate of HSO_4^- is mainly due to the low volatility and highly hygroscopic properties of sulfate (G. H. Wang et al., 2022; S. P. Zhang et al., 2019; Sun et al., 2013). Compared with that during E2 (slope $= 0.014$), the decreased formation rate of HSO_4^- during E1 (slope $= 0.009$) may be because of the decreases in aerosol acidity with higher RH (> 80 %; Huang et al., 2019; Meng et al., 2014; Tian et al., 2021). And the increased contributions of regional transport due to the high WS (2.4 ± 0.8 m s^{-1}) during E2 are compared with the low WS (0.08 ± 0.08 m s^{-1}) during E1 (Fig. S9). The fair production rates of NH_4^+ during E1 (slope $= 0.005$) and E2 (slope $= 0.006$) demonstrate that an aqueous-phase reaction could effectively promote ammonium formation. Meanwhile, a slightly larger slope of NH_4^+ during E2 could also be affected by the increased contributions of regional transport. Compared with those during E1, the inverse generation rates of two secondary organic species (i.e. $C_2H_3O^+$ and $HC_2O_4^-$) during E2 are possibly caused by the different formation pathways with a variety of RH levels or distinct regional transports. For example, $C_2H_3O^+$ shows a strong correlation with RH
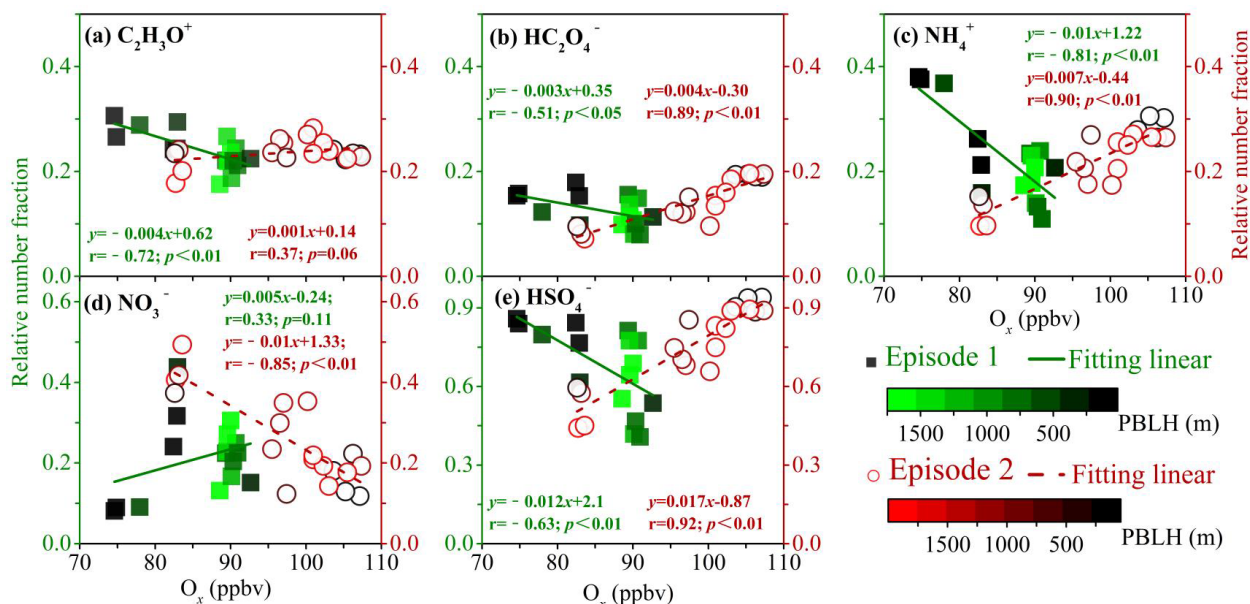
Figure 6. Correlations between the relative number fractions of the secondary species **(a)** $^{43}C_2H_3O^+$, **(b)** $^{89}HC_2O_4^-$, **(c)** $^{18}NH_4^+$, **(d)** $^{62}NO_3^-$, and **(e)** $^{97}HSO_4^-$ and O_x concentration during E1 (blue square) and E2 (red dot).

($r = 0.70$, $p < 0.05$) during E1 (slope $= 0.003$) but has an insignificant correlation during E2. This could be explained by high RHs that could effectively promote secondary organic formation during E1. In addition, the $HC_2O_4^-$ fraction increases slightly (9.7 %–13.1 %) during E1, which is potentially ascribed to more abundant dust-type particles (20.3 %), which are composed of high calcium (Ca) content (Fig. S14) and favour the formation of metal oxalate complexes (i.e. Ca oxalate). At high RHs (93.4 ± 7.6 %), if oxalate ions are dissolved in the aqueous phase with the presence of Ca ions, the Ca oxalate complexes can precipitate because of their low hygroscopicity and insoluble nature (Furukawa and Takahashi, 2011). This could offset the oxalate formation in the aqueous-phase reaction. However, significant linear increases (slope $= 0.003$) with RH ($r = 0.81$, $p < 0.01$) during E2 demonstrate that the aqueous-phase reaction effectively promotes the oxalate formation (Cheng et al., 2017; Meng et al., 2020). No significant correlation between $^{62}NO_3^-$ and RH is found during E1, potentially attributed to the decreases in NO_2 concentration (3.7 ± 0.4 ppbv) in the local atmosphere. Meanwhile, high RHs could promote organonitrate formation (Fang et al., 2021; Fry et al., 2014). The linearity between $^{62}NO_3^-$ and RH ($r = 0.69$, $p < 0.01$) significantly decreases during E2, mostly due to the losses of the volatile compound through regional transport (Fig. S15).

4　Conclusions

This study presents the chemical composition, size distribution, mixing state, and secondary formation of individual par-

ticles in the south-eastern margin of the TP, China, during the pre-monsoon season using a high-resolution SPAMS. The finding shows that the K-rich (30.9 %) and BB types (18.7 %) are the two dominant aerosol particles in the remote area, followed by the OC (12.8 %), ammonium (11.9 %), aged-EC (10.9 %), and dust (10.7 %) types; the NaK-SN, metal, and other particle types contributed 0.3 %–2.8 % of the total ambient particles. By interpreting the mass spectra and diurnal trends, the major particle types are mainly from traffic emissions, biomass burning, secondary formation, and fly ash, while the dynamics of the PBL height could also affect their contributions. The observed change in the number fraction of the particle types was mainly influenced by air mass (97.61 % of the total trajectories) from north-eastern Myanmar and significantly contributed to the K-rich and BB types. The particle types show distinct size distributions. The two critical particle types, the K-rich and BB types, appear in a unimodal pattern; the fractions of OC and aged-EC particles gradually decrease with the increase in particle size, but the ammonium and dust types show the opposite trend. Sulfate is the major secondary species and is highly mixed with the K-rich, ammonium, and aged-EC types. Nitrate has a relatively low mixing ratio due to its higher volatility than sulfate during regional transportation, while the relatively high fraction of nitrate in the BB and OC types is mainly affected by the sources of vehicle exhaust and biomass burning as well as ageing degree. During the entire study campaign, two episodes with high number concentrations of particles occur but with significant differences in each particle fraction due to the different meteorological conditions (RH, WS, etc.).
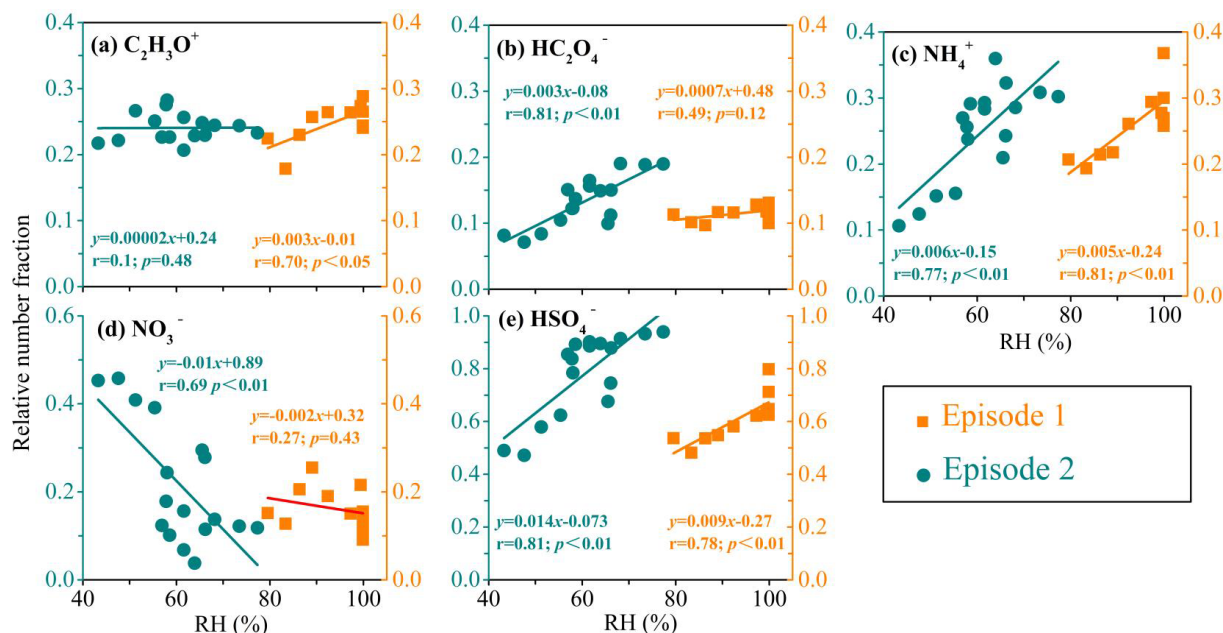
Figure 7. Correlations between the relative number fractions of the secondary species **(a)** $^{43}C_2H_3O^+$, **(b)** $^{89}HC_2O_4^-$, **(c)** $^{18}NH_4^+$, **(d)** $^{62}NO_3^-$, and **(e)** $^{97}HSO_4^-$ and relative humidity (RH) during E1 (cyan dot) and E2 (orange square).

Meanwhile, the different meteorological conditions also lead to an inverse linear correlation between the indicators of secondary formation, including $C_2H_3O^+$, $HC_2O_4^-$, NH_4^+, NO_3^-, and HSO_4^- as well as O_x (O_3+NO_2) during the periods of Episodes 1 and 2; however, they present a positive linear correlation with relative humidity (RH), except for NO_3^-, which shows a negative linear correlation with RH due to the low precursor concentration and potential organonitrate formation. These results demonstrate that the capacity of atmospheric ageing of photooxidation and aqueous reaction has complex influencing factors. Although the detailed formation pathways and their percentage contributions to secondary species are not quantitatively estimated in this study, our results have important implications for the various possibilities affecting the characteristics of chemical components, size distribution, mixing states, and formation mechanism of aerosols in the south-eastern TP. More in-depth investigations concerning the evolution mechanisms of secondary aerosols are encouraged since the TP is a significant regulator of global climate change.

Author contributions. QW and JC designed the campaign. WR conducted field measurements. LL, QW, JT, and YZ performed data analysis and interpretation. LL and QW wrote the paper. All the authors reviewed and commented on the paper.

References

Alexander, B., Hastings, M. G., Allman, D. J., Dachs, J., Thornton, J. A., and Kunasek, S. A.: Quantifying atmospheric nitrate formation pathways based on a global model of the oxygen isotopic composition (Δ^{17}O) of atmospheric nitrate, Atmos. Chem. Phys., 9, 5043–5056, https://doi.org/10.5194/acp-9-5043-2009, 2009.

Allen, J. O., Fergenson, D. P., Gard, E. E., Hughes, L. S., Morrical, B. D., Kleeman, M. J., Gross, D. S., Gälli, M. E., Prather, K. A., and Cass, G. R.: Particle Detection Efficiencies of Aerosol Time of Flight Mass Spectrometers under Ambient Sampling Conditions, Environ. Sci. Technol., 34, 211–217, https://doi.org/10.1021/es9904179, 2000.

Aruffo, E., Wang, J., Ye, J., Ohno, P., Qin, Y., Stewart, M., McKinney, K., Di Carlo, P., and Martin, S. T.: Partitioning of Organonitrates in the Production of Secondary Organic Aerosols from α-Pinene Photo-Oxidation, Environ. Sci. Technol., 56, 5421–5429, https://doi.org/10.1021/acs.est.1c08380, 2022.

Bi, X. H., Zhang, G. H., Li, L., Wang, X. M., Li, M., Sheng, G. Y., Fu, J. M., and Zhou, Z.: Mixing state of biomass burning particles by single particle aerosol mass spectrometer in the urban area of PRD, China, Atmos. Environ., 45, 3447–3453, https://doi.org/10.1016/j.atmosenv.2011.03.034, 2011.

Bi, X. H., Lin, Q. H., Peng, L., Zhang, G. H., Wang, X. M., Brechtel, F. J., Chen, D. H., Li, M., Peng, P. A., Sheng, G. Y., and Zhou, Z.: In situ detection of the chemistry of individual fog droplet residues in the Pearl River Delta region, China, J. Geophys. Res.-Atmos., 121, 9105–9116, https://doi.org/10.1002/2016jd024886, 2016.

Budisulistiorini, S. H., Riva, M., Williams, M., Chen, J., Itoh, M., Surratt, J. D., and Kuwata, M.: Light-absorbing brown carbon aerosol constituents from combustion of Indonesian peat and biomass, Environ. Sci. Technol., 51, 4415–4423, https://doi.org/10.1021/acs.est.7b00397, 2017.

Cahill, J. F., Suski, K., Seinfeld, J. H., Zaveri, R. A., and Prather, K. A.: The mixing state of carbonaceous aerosol particles in northern and southern California measured during CARES and CalNex 2010, Atmos. Chem. Phys., 12, 10989–11002, https://doi.org/10.5194/acp-12-10989-2012, 2012.

Canagaratna, M. R., Jayne, J. T., Jimenez, J. L., Allan, J. D., Alfarra, M. R., Zhang, Q., Onasch, T. B., Drewnick, F., Coe, H., Middlebrook, A., Delia, A., Williams, L. R., Trimborn, A. M., Northway, M. J., DeCarlo, P. F., Kolb, C. E., Davidovits, P., and Worsnop, D. R.: Chemical and microphysical characterization of ambient aerosols with the aerodyne aerosol mass spectrometer, Mass Spectrom. Rev., 26, 185–222, https://doi.org/10.1002/mas.20115, 2007.

Chan, C. Y., Wong, K. H., Li, Y. S., Chan, Y., and Zhang, X. D.: The effects of Southeast Asia fire activities on tropospheric ozone, trace gases and aerosols at a remote site over the Tibetan Plateau of Southwest China, Tellus B, 58, 310–318, https://doi.org/10.1111/j.1600-0889.2006.00187.x, 2017.

Chen, J. Q. and Bordoni, S.: Orographic effects of the Tibetan Plateau on the East Asian Summer Monsoon: An energetic perspective, J. Climate, 27, 3052–3072, https://doi.org/10.1175/JCLI-D-13-00479.1, 2014.

Chen, Y., Cao, J. J., Huang, R. J., Yang, F. M., Wang, Q. Y., and Wang, Y. C.: Characterization, mixing state, and evolution of urban single particles in Xi'an (China) during wintertime haze days, Sci. Total Environ., 573, 937–945, https://doi.org/10.1016/j.scitotenv.2016.08.151, 2016.

Chen, Y., Wenger, J. C., Yang, F. M., Cao, J. J., Huang, R. J., Shi, G. M., Zhang, S. M., Tian, M., and Wang, H. B.: Source characterization of urban particles from meat smoking activities in Chongqing, China using single particle aerosol mass spectrometry, Environ. Pollut., 228, 92–101, https://doi.org/10.1016/j.envpol.2017.05.022, 2017.

Chen, Y., Tian, M., Huang, R.-J., Shi, G., Wang, H., Peng, C., Cao, J., Wang, Q., Zhang, S., Guo, D., Zhang, L., and Yang, F.: Characterization of urban amine-containing particles in southwestern China: seasonal variation, source, and processing, Atmos. Chem. Phys., 19, 3245–3255, https://doi.org/10.5194/acp-19-3245-2019, 2019.

Cheng, C., Li, M., Chan, C. K., Tong, H., Chen, C., Chen, D., Wu, D., Li, L., Wu, C., Cheng, P., Gao, W., Huang, Z., Li, X., Zhang, Z., Fu, Z., Bi, Y., and Zhou, Z.: Mixing state of oxalic acid containing particles in the rural area of Pearl River Delta, China: implications for the formation mechanism of oxalic acid, Atmos. Chem. Phys., 17, 9519–9533, https://doi.org/10.5194/acp-17-9519-2017, 2017.

Crippa, M., DeCarlo, P. F., Slowik, J. G., Mohr, C., Heringa, M. F., Chirico, R., Poulain, L., Freutel, F., Sciare, J., Cozic, J., Di Marco, C. F., Elsasser, M., Nicolas, J. B., Marchand, N., Abidi, E., Wiedensohler, A., Drewnick, F., Schneider, J., Borrmann, S., Nemitz, E., Zimmermann, R., Jaffrezo, J.-L., Prévôt, A. S. H., and Baltensperger, U.: Wintertime aerosol chemical composition and source apportionment of the organic fraction in the metropolitan area of Paris, Atmos. Chem. Phys., 13, 961–981, https://doi.org/10.5194/acp-13-961-2013, 2013.

Dall'Osto, M. and Harrison, R. M.: Urban organic aerosols measured by single particle mass spectrometry in the megacity of London, Atmos. Chem. Phys., 12, 4127–4142, https://doi.org/10.5194/acp-12-4127-2012, 2012.

Dall'Osto, M., Beddows, D. C. S., Gietl, J. K., Olatunbosun, O. A., Yang, X. G., and Harrison, R. M.: Characteristics of tyre dust in polluted air: studies by single particle mass spectrometry (ATOFMS), Atmos. Environ., 94, 224–230, https://doi.org/10.1016/j.atmosenv.2014.05.026, 2014.

Ding, J., Dai, Q. L., Zhang, Y. F., Xu, J., Huangfu, Y. Q., and Feng, Y. C.: Air humidity affects secondary aerosol formation in different pathways, Sci. Total Environ., 759, 143540–143549, https://doi.org/10.1016/j.scitotenv.2020.143540, 2021.

Draxler, R. and Hess, G.: An overview of the HYSPLIT_4 modelling system for trajectories, Aust. Meteorol. Mag., 47, 295–308, 1998.

Du, W., Sun, Y. L., Xu, Y. S., Jiang, Q., Wang, Q. Q., Yang, W., Wang, F., Bai, Z. P., Zhao, X. D., and Yang, Y. C.: Chemical characterization of submicron aerosol and particle growth events at a national background site (3295 m a.s.l.) on

the Tibetan Plateau, Atmos. Chem. Phys., 15, 10811–10824, https://doi.org/10.5194/acp-15-10811-2015, 2015.

Engling, G., Zhang, Y. N., Chan, C. Y., Sang, X. F., Lin, M., Ho, K. F., Li, Y. S., Lin, C. Y., and Lee, J. J.: Characterization and sources of aerosol particles over the southeastern Tibetan Plateau during the Southeast Asia biomass-burning season, Tellus B, 63, 117–128, https://doi.org/10.1111/j.1600-0889.2010.00512.x, 2011.

Ervens, B., Turpin, B. J., and Weber, R. J.: Secondary organic aerosol formation in cloud droplets and aqueous particles (aq-SOA): a review of laboratory, field and model studies, Atmos. Chem. Phys., 11, 11069–11102, https://doi.org/10.5194/acp-11-11069-2011, 2011.

Fang, X. Z., Liu, Y. Y., Li, K. J., Wang, T., Deng, Y., Feng, Y. Q., Yang, Y., Cheng, H. Y., Chen, J. M., and Zhang, L. W.: Atmospheric Nitrate Formation through Oxidation by Carbonate Radical, ACS Earth Space Chem., 5, 1801–1811, https://doi.org/10.1021/acsearthspacechem.1c00169, 2021.

Fry, J. L., Draper, D. C., Barsanti, K. C., Smith, J. N., Ortega, J., Winkler, P. M., Lawler, M. J., Brown, S. S., Edwards, P. M., Cohen, R. C., and Lee, L.: Secondary Organic Aerosol Formation and Organic Nitrate Yield from NO_3 Oxidation of Biogenic Hydrocarbons, Environ. Sci. Technol., 48, 11944–11953, https://doi.org/10.1021/es502204x, 2014.

Furukawa, T. and Takahashi, Y.: Oxalate metal complexes in aerosol particles: implications for the hygroscopicity of oxalate-containing particles, Atmos. Chem. Phys., 11, 4289–4301, https://doi.org/10.5194/acp-11-4289-2011, 2011.

Gettelman, A., Morrison, H., Terai, C. R., and Wood, R.: Corrigendum to "Microphysical Process Rates and Global Aerosol-Cloud Interactions" published in Atmos. Chem. Phys., 13, 9855–9867, 2013, Atmos. Chem. Phys., 14, 9099–9103, https://doi.org/10.5194/acp-14-9099-2014, 2013.

Han, H., Wu, Y., Liu, J., Zhao, T., Zhuang, B., Wang, H., Li, Y., Chen, H., Zhu, Y., Liu, H., Wang, Q., Li, S., Wang, T., Xie, M., and Li, M.: Impacts of atmospheric transport and biomass burning on the inter-annual variation in black carbon aerosols over the Tibetan Plateau, Atmos. Chem. Phys., 20, 13591–13610, https://doi.org/10.5194/acp-20-13591-2020, 2020.

Healy, R. M., Sciare, J., Poulain, L., Crippa, M., Wiedensohler, A., Prévôt, A. S. H., Baltensperger, U., Sarda-Estève, R., McGuire, M. L., Jeong, C.-H., McGillicuddy, E., O'Connor, I. P., Sodeau, J. R., Evans, G. J., and Wenger, J. C.: Quantitative determination of carbonaceous particle mixing state in Paris using single-particle mass spectrometer and aerosol mass spectrometer measurements, Atmos. Chem. Phys., 13, 9479–9496, https://doi.org/10.5194/acp-13-9479-2013, 2013.

Hua, S., Liu, Y. Z., Luo, R., Shao, T. B., and Zhu, Q. Z.: Inconsistent aerosol indirect effects on water clouds and ice clouds over the Tibetan Plateau, Int. J. Climatol., 40, 3832–3848, https://doi.org/10.1002/joc.6430, 2019.

Huang, X. J., Zhang, J. K., Luo, B., Luo, J. Q., Zhang, W., and Rao, Z. H.: Characterization of oxalic acid-containing particles in summer and winter seasons in Chengdu China, Atmos. Environ., 198, 133–141, https://doi.org/10.1016/j.atmosenv.2018.10.050, 2019.

Immerzeel, W. W., van Beek, L. P. H., and Bierkens, M. F. P.: Climate change will affect the Asian water towers, Science, 328, 1382–1385, https://doi.org/10.1126/science.1183188, 2010.

Jacobson, M. Z.: Analysis of aerosol interactions with numerical techniques for solving coagulation, nucleation, condensation, dissolution, and reversible chemistry among multiple size distributions, J. Geophys. Res., 107, 4366, https://doi.org/10.1029/2001JD002044, 2002.

Jiang, H. H., Frie, A. L., Lavi, A., Chen, J. Y., Zhang, H., Bahreini, R., and Lin, Y. H.: Brown carbon formation from nighttime chemistry of unsaturated heterocyclic volatile organic compounds, Environ. Sci. Tech. Let., 6, 184190, https://doi.org/10.1021/acs.estlett.9b00017, 2019.

Kumar, M., Raju, M. P., Singh, R. K., Singh, A. K., Singh, R. S., and Banerjee, T.: Wintertime characteristics of aerosols over middle Indo-Gangetic Plain: vertical profile, transport and radiative forcing, Atmos. Res., 183, 268–282, https://doi.org/10.1016/j.atmosres.2016.09.012, 2017.

Kundu, S., Kawamura, K., Andreae, T. W., Hoffer, A., and Andreae, M. O.: Molecular distributions of dicarboxylic acids, ketocarboxylic acids and α-dicarbonyls in biomass burning aerosols: implications for photochemical production and degradation in smoke layers, Atmos. Chem. Phys., 10, 2209–2225, https://doi.org/10.5194/acp-10-2209-2010, 2010.

Li, C. L., Bosch, C., Kang, S. C., Andersson, A., Chen, P. F., Zhang, Q. G., Cong, Z. Y., Chen, B., Qin, D. H., and Gustafsson, Ö.: Sources of black carbon to the Himalayan–Tibetan Plateau glaciers, Nat. Commun., 7, 12574, https://doi.org/10.1038/ncomms12574, 2016.

Li, C. L., Bosch, C., Kang, S. C., Andersson, A., Chen, P. F., Zhang, Q. G., Cong, Z. Y., Tripathee, L., and Örjanb, G.: ^{14}C characteristics of organic carbon in the atmosphere and at glacier region of the Tibetan Plateau, Sci. Total Environ., 832, 155020, https://doi.org/10.1016/j.scitotenv.2022.155020, 2022.

Li, J. J., Wang, G. H., Wang, X. M., Cao, J. J., Sun, T., Cheng, C. L., Meng, J. J., Hu, T. F., and Liu, S. X.: Abundance, composition and source of atmospheric $PM_{2.5}$ at a remote site in the Tibetan Plateau, China, Tellus B, 65, 20281, https://doi.org/10.3402/tellusb.v65i0.20281, 2013.

Li, L., Huang, Z. X., Dong, J. G., Li, M., Gao, W., Nian, H. Q., Fu, Z., Zhang, G. H., Bi, X. H., Cheng, P., and Zhou, Z.: Real time bipolar time-of-flight mass spectrometer for analyzing single aerosol particles, Int. J. Mass Spectrom., 303, 118–124, https://doi.org/10.1016/j.ijms.2011.01.017, 2011.

Li, L., Wang, Q. Y., Zhang, Y., Liu, S. X., Zhang, T., Wang, S., Tian, J., Chen, Y., Hang Ho, S. S., Han, Y., and Cao, J. J.: Impact of reduced anthropogenic emissions on chemical characteristics of urban aerosol by individual particle analysis, Chemosphere, 303, 135013, https://doi.org/10.1016/j.chemosphere.2022.135013, 2022a.

Li, L., Wang, Q., Tian, J., Liu, H., Zhang, Y., Sai Hang Ho, S., Ran, w., and Cao, J.: In-depth study of the formation processes of single atmospheric particles in the southeastern margin of Tibetan Plateau, Version 1, Zenodo [data set], https://doi.org/10.5281/zenodo.7336857, 2022b.

Li, Y. J., Sun, Y. L., Zhang, Q., Li, X., Li, M., Zhou, Z., and Chan, C. K.: Real-time chemical characterization of atmospheric particulate matter in China: A review, Atmos. Environ., 158, 270–304, https://doi.org/10.1016/j.atmosenv.2017.02.027, 2017.

Liang, Z. C., Zhou, L. Y., Cuevas, R. A., Li, X. Y., Cheng, C. L., Li, M., Tang, R. Z., Zhang, R. F., Lee, P. K. H., Lai, A. C. K., and Chan, C. K.: Sulfate Formation in Incense Burning Particles:

A Single-Particle Mass Spectrometric Study, Environ. Sci. Tech. Let., 9, 718–725, https://doi.org/10.1021/acs.estlett.2c00492, 2022.

Lin, Q., Bi, X., Zhang, G., Yang, Y., Peng, L., Lian, X., Fu, Y., Li, M., Chen, D., Miller, M., Ou, J., Tang, M., Wang, X., Peng, P., Sheng, G., and Zhou, Z.: In-cloud formation of secondary species in iron-containing particles, Atmos. Chem. Phys., 19, 1195–1206, https://doi.org/10.5194/acp-19-1195-2019, 2019.

Link, M. F., Kim, J., Park, G., Lee, T., Park, T., Babar, Z. B., Sung, K., Kim, P., Kang, S., Kim, J. S., Choi, Y., Son, J., Lim, H. J., and Farmer, D. K.: Elevated production of NH_4NO_3 from the photochemical processing of vehicle exhaust: Implications for air quality in the Seoul Metropolitan Region, Atmos. Environ., 156, 95–101, https://doi.org/10.1016/j.atmosenv.2017.02.031, 2017.

Liu, D. T., Hu, K., Zhao, D. L., Ding, S., Wu, Y. F., Zhou, C., Yu, C. J., Tian, P., Liu, Q., Bi, K., Wu, Y. Z., Hu, B., Ji, D. S., Kong, S. F., Ouyang, B., He, H., Huang, M. Y., and Ding, D.P.: Efficient Vertical Transport of Black Carbon in the Planetary Boundary Layer, Geophys. Res. Lett., 47, e2020GL088858, https://doi.org/10.1029/2020GL088858, 2020.

Liu, H., Wang, Q., Xing, L., Zhang, Y., Zhang, T., Ran, W., and Cao, J.: Measurement report: quantifying source contribution of fossil fuels and biomass-burning black carbon aerosol in the south-eastern margin of the Tibetan Plateau, Atmos. Chem. Phys., 21, 973–987, https://doi.org/10.5194/acp-21-973-2021, 2021.

Liu, Q., Liu, D., Gao, Q., Tian, P., Wang, F., Zhao, D., Bi, K., Wu, Y., Ding, S., Hu, K., Zhang, J., Ding, D., and Zhao, C.: Vertical characteristics of aerosol hygroscopicity and impacts on optical properties over the North China Plain during winter, Atmos. Chem. Phys., 20, 3931–3944, https://doi.org/10.5194/acp-20-3931-2020, 2020.

Liu, X. D., Dong, B. W., Yin, Z. Y., Smith, R. S., and Guo, Q. C.: Continental drift and plateau uplift control origination and evolution of Asian and Australian monsoons, Scientific Reports, 7, 40344, https://doi.org/10.1038/srep40344, 2017.

Luo, M., Liu, Y. Z., Zhu, Q. Z., Tang, Y. H., and Alam, K.: Role and mechanisms of black carbon affecting water vapor transport to Tibet, Remote Sensing, 12, 231, https://doi.org/10.3390/rs12020231, 2020.

Ma, X., Yu, F., and Luo, G.: Aerosol direct radiative forcing based on GEOS-Chem-APM and uncertainties, Atmos. Chem. Phys., 12, 5563–5581, https://doi.org/10.5194/acp-12-5563-2012, 2012.

Matsui, H.: Black carbon simulations using a size- and mixingstate-resolved three-dimensional model: 2. Aging timescale and its impact over East Asia, J. Geophys. Res.-Atmos., 121, 1808–1821, https://doi.org/10.1002/2015jd023999, 2016.

Meng, J. J, Wang, G. H, Li, J. J, Cheng, C. L, Ren, Y. Q, Huang, Y., Cheng, Y. T., Cao, J. J., and Zhang, T.: Seasonal characteristics of oxalic acid and related SOA in the free troposphere of Mt. Hua, central China: implications for sources and formation mechanisms, Sci. Total Environ., 493, 1088–1097, https://doi.org/10.1016/j.scitotenv.2014.04.086, 2014.

Meng, J. J., Liu, X. D., Hou, Z. F., Yi, Y. N., Yan, L., Li, Z., Cao, J. J., Li, J. J., and Wang, G. H.: Molecular characteristics and stable carbon isotope compositions of dicarboxylic acids and related compounds in the urban atmosphere of the North China Plain: implications for aqueous phase formation of SOA during the haze periods, Sci. Total Environ., 705, 135256, https://doi.org/10.1016/j.scitotenv.2019.135256, 2020.

National Centers for Environmental Prediction, National Weather Service, NOAA, and U.S. Department of Commerce: NCEP FNL Operational Model Global Tropospheric Analyses, continuing from July 1999, Research Data Archive at the National Center for Atmospheric Research, Computational and Information Systems Laboratory [data set], https://doi.org/10.5065/D6M043C6, 2000.

Ng, N. L., Canagaratna, M. R., Jimenez, J. L., Chhabra, P. S., Seinfeld, J. H., and Worsnop, D. R.: Changes in organic aerosol composition with aging inferred from aerosol mass spectra, Atmos. Chem. Phys., 11, 6465–6474, https://doi.org/10.5194/acp-11-6465-2011, 2011.

Peng, J. F., Hu, M., Guo, S., Du, Z. F., Zheng, J., Shang, D. J., Zamora, M. L., Zeng, L. M., Shao, M., Wu, Y. S., Zheng, J., Wang, Y., Glen, C. R., Collins, D. R., Molina, M. J., and Zhang, R. Y.: Markedly enhanced absorption and direct radiative forcing of black carbon under polluted urban environments, P. Natl. Acad. Sci. USA, 113, 4266–4271, https://doi.org/10.1073/pnas.1602310113, 2016.

Pratt, K. A., Murphy, S. M., Subramanian, R., DeMott, P. J., Kok, G. L., Campos, T., Rogers, D. C., Prenni, A. J., Heymsfield, A. J., Seinfeld, J. H., and Prather, K. A.: Flight-based chemical characterization of biomass burning aerosols within two prescribed burn smoke plumes, Atmos. Chem. Phys., 11, 12549–12565, https://doi.org/10.5194/acp-11-12549-2011, 2011.

Qian, Y., Flanner, M. G., Leung, L. R., and Wang, W.: Sensitivity studies on the impacts of Tibetan Plateau snowpack pollution on the Asian hydrological cycle and monsoon climate, Atmos. Chem. Phys., 11, 1929–1948, https://doi.org/10.5194/acp-11-1929-2011, 2011.

Rehbein, P. J., Jeong, C. H., McGuire, M. L., Yao, X., Corbin, J. C., and Evans, G. J.: Cloud and fog processing enhanced gastoparticle partitioning of trimethylamine, Environ. Sci. Technol., 45, 4346–4352, https://doi.org/10.1021/es1042113, 2011.

Roth, A., Schneider, J., Klimach, T., Mertes, S., van Pinxteren, D., Herrmann, H., and Borrmann, S.: Aerosol properties, source identification, and cloud processing in orographic clouds measured by single particle mass spectrometry on a central European mountain site during HCCT-2010, Atmos. Chem. Phys., 16, 505–524, https://doi.org/10.5194/acp-16-505-2016, 2016.

Shen, L. J., Wang, H. L., Lü, S., Zhang, X. H., Yuan, J., Tao, S. K., Zhang, G. J., Wang, F., and Li, L.: In?uence of pollution control on air pollutants and the mixing state of aerosol particles during the 2nd World Internet Conference in Jiaxing, China, J. Clean. Prod., 149, 436–447, https://doi.org/10.1016/j.jclepro.2017.02.114, 2017.

Shen, R.-Q., Ding, X., He, Q.-F., Cong, Z.-Y., Yu, Q.-Q., and Wang, X.-M.: Seasonal variation of secondary organic aerosol tracers in Central Tibetan Plateau, Atmos. Chem. Phys., 15, 8781–8793, https://doi.org/10.5194/acp-15-8781-2015, 2015.

Sirois, A. and Bottenheim, J. W.: Use of backward trajectories to interpret the 5-year record of PAN and O_3 ambient air concentrations at Kejimkujik National Park, Nova Scotia, J. Geophys. Res., 100, 2867–2881, https://doi.org/10.1029/94JD02951, 1995.

Song, X. H. and Hopke, P. K.: Classifcation of single particles analyzed by ATOFMS using an artifcial neural network, ART-2A,

Anal. Chem., 71, 860–865, https://doi.org/10.1021/ac9809682, 1999.

Sorooshian, A., Lu, M. L., Brechtel, F. J., Jonsson, H., Feingold, G., Flagan, R. C., and Seinfeld, J. H.: On the source of organic acid aerosol layers above clouds, Environ. Sci. Technol., 41, 4647–4654, https://doi.org/10.1021/es0630442, 2007.

Sullivan, R. C., Guazzotti, S. A., Sodeman, D. A., and Prather, K. A.: Direct observations of the atmospheric processing of Asian mineral dust, Atmos. Chem. Phys., 7, 1213–1236, https://doi.org/10.5194/acp-7-1213-2007, 2007.

Sun, Y. L, Wang, Z. F., Fu, P. Q., Jiang, Q. J., Yang, T., Li, J., and Ge, X. L.: The impact of relative humidity on aerosol composition and evolution processes during wintertime in Beijing, China, Atmos. Environ., 77, 927–934, https://doi.org/10.1016/j.atmosenv.2013.06.019, 2013.

Tian, J., Wang, Q. Y., Zhang, Y., Yan, M. Y., Liu, H. K., Zhang, N. N., Ran, W. K., and Cao, J. J.: Impacts of primary emissions and secondary aerosol formation on air pollution in an urban area of China during the COVID-19 lockdown, Environ. Int., 150, 106426–14, https://doi.org/10.1016/j.envint.2021.106426, 2021.

Wang, A. Q., Xie, X. N., Liu, X. D., and Yin, Z. Y.: Direct Radiative Effect (DRE) of Dust Aerosols on West African and East Asian Monsoon: The Role of Ocean-Atmosphere Interactions, J. Geophys. Res.-Atmos., 127, 1–20, https://doi.org/10.1029/2021JD035917, 2022.

Wang, G. H., Zhang, R. Y., Gomez, M. E., Yang, L. X., Zamora, M. L., Hu, M., Lin, Y., Peng, J. F., Guo, S., Meng, J. J., Li, J. J., Cheng, C. L., Hu, T. F., Ren, Y. Q., Wang, Y. S., Gao, J., Cao, J. J., An, Z. S., Zhou, W. J., Li, G. H., Wang, J. Y., Tian, P. F., Marrero-Ortiz, W., Secrest, J., Du, Z. F., Zheng, J., Shang, D. J., Zeng, L. M., Shao, M., Wang, W. G., Huang, Y., Wang, Y., Zhu, Y. J., Li, Y. X., Hu, J. X., Pan, B. W., Cai, L., Cheng, Y. T., Ji, Y. M., Zhang, Y., Rosenfeld, D., Liss, P. S., Duce, R. A., Kolb, C. E., and Molina, M. J.: Persistent sulfate formation from London Fog to Chinese haze, P. Natl. Acad. Sci. USA, 113, 13630–13635, https://doi.org/10.1073/pnas.1616540113, 2016.

Wang, H. C., Lu, K. D., Chen, X. R., Zhu, Q. D., Chen, Q., Guo, S., Jiang, M. Q., Li, X., Shang, D. J., Tan, Z. F., Wu, Y. S., Wu, Z. J., Zou, Q., Zheng, Y., Zeng, L. M., Zhu, T., Hu, M., and Zhang, Y. H.: High N_2O_5 concentrations observed in urban Beijing: implications of a large nitrate formation pathway, Environ. Sci. Tech. Let., 4, 416–420, https://doi.org/10.1021/acs.estlett.7b00341, 2017.

Wang, H. L., An, J. L., Shen, L. J., Zhu, B., Xia, L., Duan, Q., and Zou, J. N.: Mixing state of ambient aerosols in Nanjing city by single particle mass spectrometry, Atmos. Environ., 132, 123–132, https://doi.org/10.1016/j.atmosenv.2016.02.032, 2016.

Wang, H. L., Shen, L. J., Yin, Y., Chen, K., Chen, J. H., and Wang, Y. S.: Characteristics and mixing state of aerosol at the summit of Mount Tai (1534 m) in Central East China: First measurements with SPAMS, Atmos. Environ., 213, 273–284, https://doi.org/10.1016/j.atmosenv.2019.06.021, 2019.

Wang, Q. Y., Han, Y. M., Ye, J. H., Liu, S. X., Pongpiachan, S., Zhang, N. N., Han, Y. M., Tian, J., Wu, C., Long, X., Zhang, Q., Zhang, W. Y., Zhao, Z. Z., and Cao, J. J.: High contribution of secondary brown carbon to aerosol light absorption in the southeastern margin of Tibetan Plateau, Geophys. Res. Lett., 46, 4962–4970, https://doi.org/10.1029/2019GL082731, 2019.

Wenzel, R. J., Liu, D.-Y., Edgerton, E. S., and Prather, K. A.: Aerosol time-of-flight mass spectrometry during the Atlanta Supersite Experiment: 2. Scaling procedures, J. Geophys. Res., 108, 8427, https://doi.org/10.1029/2001jd001563, 2003.

Wood, E. C., Canagaratna, M. R., Herndon, S. C., Onasch, T. B., Kolb, C. E., Worsnop, D. R., Kroll, J. H., Knighton, W. B., Seila, R., Zavala, M., Molina, L. T., DeCarlo, P. F., Jimenez, J. L., Weinheimer, A. J., Knapp, D. J., Jobson, B. T., Stutz, J., Kuster, W. C., and Williams, E. J.: Investigation of the correlation between odd oxygen and secondary organic aerosol in Mexico City and Houston, Atmos. Chem. Phys., 10, 8947–8968, https://doi.org/10.5194/acp-10-8947-2010, 2010.

Xu, L. L., Wu, X., Hong, Z. Y., Zhang, Y. R., Deng, J. J., Hong, Y. W., and Chen, J. S.: Composition, mixing state, and size distribution of single submicron particles during pollution episodes in a coastal city in southeast China, Environ. Sci. Pollut. R., 26, 1464–1473, https://doi.org/10.1007/s11356-018-3469-x, 2018.

Xu, W. Q., Han, T. T., Du, W., Wang, Q. Q., Chen, C., Zhao, J., Zhang, Y. J., Li, J., Fu, P. Q., Wang, Z. F., Worsnop, D. R., and Sun, Y. L.: Effects of aqueous-phase and photochemical processing on secondary organic aerosol formation and evolution in Beijing, China, Environ. Sci. Technol., 51, 762–770, https://doi.org/10.1021/acs.est.6b04498, 2017.

Xue, J., Griffth, S. M., Yu, X., Lau, A. K. H., and Yu, J. Z.: Effect of nitrate and sulfate relative abundance in $PM_{2.5}$ on liquid water content explored through half-hourly observations of inorganic soluble aerosols at a polluted receptor site, Atmos. Environ., 99, 24–31, https://doi.org/10.1016/j.atmosenv.2014.09.049, 2014.

Yang, J., Ma, S. X., Gao, B., Li, X. Y., Zhang, Y. J., Cai, J., Li, M., Yao, L. A., Huang, B., and Zheng, M.: Single particle mass spectral signatures from vehicle exhaust particles and the source apportionment of on-line $PM_{2.5}$ by single particle aerosol mass spectrometry, Sci. Total Environ., 593, 310–318, https://doi.org/10.1016/j.scitotenv.2017.03.099, 2017.

Zauscher, M. D., Wang, Y., Moore, M. J. K., Gaston, C. J., and Prather, K. A.: Air Quality Impact and Physicochemical Aging of Biomass Burning Aerosols during the 2007 San Diego Wildfires, Environ. Sci. Technol., 47, 7633–7643, https://doi.org/10.1021/es4004137, 2013.

Zaveri, R. A., Barnard, J., Easter, R., Riemer, N., and West, M.: Particle-resolved simulation of aerosol size, composition, mixing state, and the associated optical and cloud condensation nuclei activation properties in an evolving urban plume, J. Geophys. Res., 115, D17210, https://doi.org/10.1029/2009JD013616, 2010.

Zhang, G., Lin, Q., Peng, L., Yang, Y., Fu, Y., Bi, X., Li, M., Chen, D., Chen, J., Cai, Z., Wang, X., Peng, P., Sheng, G., and Zhou, Z.: Insight into the in-cloud formation of oxalate based on in situ measurement by single particle mass spectrometry, Atmos. Chem. Phys., 17, 13891–13901, https://doi.org/10.5194/acp-17-13891-2017, 2017.

Zhang, G., Lian, X., Fu, Y., Lin, Q., Li, L., Song, W., Wang, Z., Tang, M., Chen, D., Bi, X., Wang, X., and Sheng, G.: High secondary formation of nitrogen-containing organics (NOCs) and its possible link to oxidized organics and ammonium, Atmos. Chem. Phys., 20, 1469–1481, https://doi.org/10.5194/acp-20-1469-2020, 2020.

Zhang, G. H., Bi, X. H., Chan, L. Y., Li, L., Wang, X. M., Feng, J. L., Sheng, G. Y., Fu, J. M., Li, M., and Zhou,

Z.: Enhanced trimethylamine-containing particles during fog events detected by single particle aerosol mass spectrometry in urban Guangzhou, China, Atmos. Environ., 55, 121–126, https://doi.org/10.1016/j.atmosenv.2012.03.038, 2012.

Zhang, G. H., Han, B. X., Bi, X. H., Dai, S. X., Huang, W., Chen, D. H., Wang, X. M., Sheng, G. Y., Fu, J. M., and Zhou, Z.: Characteristics of individual particles in the atmosphere of Guangzhou by single particle mass spectrometry, Atmos. Res., 153, 286–295, https://doi.org/10.1016/j.atmosres.2014.08.016, 2015.

Zhang, G. H., Lin, Q. H., Peng, L., Yang, Y. X., Jiang, F., Liu, F. X., Song, W., Chen, D. H., Cai, Z., Bi, X. H., Miller, M., Tang, M. J., Huang, W. L., Wang, X. M., Peng, P. A., and Shen, G. Y.: Oxalate Formation Enhanced by Fe-Containing Particles and Environmental Implications, Environ. Sci. Technol., 53, 1269–1277, https://doi.org/10.1021/acs.est.8b05280, 2019.

Zhang, J. K., Luo, B., Zhang, J. Q., Ouyang, F., Song, H. Y., Liu, P. C., Cao, P., Schäfer, K., Wang, S. G., Huang, X. J., and Lin, Y. F.: Analysis of the characteristics of single atmospheric particles in Chengdu using single particle mass spectrometry, Atmos. Environ., 157, 91–100, https://doi.org/10.1016/j.atmosenv.2017.03.012, 2017.

Zhang, N. N., Cao, J. J., Xu, H. M., and Zhu, C. S.: Elemental compositions of $PM_{2.5}$ and TSP in Lijiang, southeastern edge of Tibetan Plateau during pre-monsoon period, Particuology, 11, 63–69, https://doi.org/10.1016/j.partic.2012.08.002, 2013.

Zhang, S. P., Xing, J., Sarwar, G., Ge, Y. L., He, H., Duan, F. K., Zhao, Y., He, K. B., Zhu, L. D., and Chu, B. W.: Parameterization of heterogeneous reaction of SO_2 to sulfate on dust with coexistence of NH_3 and NO_2 under different humidity conditions, Atmos. Environ., 208, 133–140, https://doi.org/10.1016/j.atmosenv.2019.04.004, 2019.

Zhang, X., Xu, J., Kang, S., Zhang, Q., and Sun, J.: Chemical characterization and sources of submicron aerosols in the northeastern Qinghai–Tibet Plateau: insights from high-resolution mass spectrometry, Atmos. Chem. Phys., 19, 7897–7911, https://doi.org/10.5194/acp-19-7897-2019, 2019.

Zhao, S. Y., Tie, X. X., Long, X., and Cao, J. J.: Impacts of Himalayas on black carbon over the Tibetan Plateau during summer monsoon, Sci. Total Environ., 598, 307–318, https://doi.org/10.1016/j.scitotenv.2017.04.101, 2017.